JOURNAL OF COMPUTATIONAL PHYSICS **123,** 96–110 (1996)
ARTICLE NO. 0008

Radiation Boundary Conditions in Barotropic Coastal Ocean Numerical Models

Y. TANG AND R. GRIMSHAW

Department of Mathematics, Monash University, Clayton, Victoria 3168, Australia

Received February 22, 1994; revised May 15, 1995

Using a barotropic coastal ocean numerical model, several radiation boundary conditions at the open boundaries of the computational domain are examined. The focus is on how well they can transmit coastally trapped waves. As well as radiation boundary conditions of the Orlanski type, three new modifications are introduced and found to give a better performance.

1. INTRODUCTION

In the numerical simulation of coastal ocean circulation open boundary conditions inevitably occur and they can play a crucial role in determining the validity of the results. Ideally numerical open boundary conditions should allow fluid motions generated in the computational domain and which are felt at the open boundary to pass through the boundary without influencing the interior solution. This is a long-standing and well-known problem and, since the advent of numerical ocean models, there have been several solutions proposed. Similar problems arise in limited-area atmospheric models and in other fluid dynamic flows. However, none of the various open boundary conditions in common use appear to be universally and ideally satisfactory (e.g., Chapman [1] and Röed and Cooper [2]). In general, while some open boundary conditions are satisfactory in a particular context they may prove unreliable in a different context.

The main motivation of this study is to identify and test radiation boundary conditions suitable for use in storm surge numerical models. We consider the usual shallow water equations in a computational domain which contains a coastline and, importantly, has bottom topography which varies in the offshore direction and is uniform in the longshore direction. This configuration allows for a full spectrum of coastally trapped waves propagating in the longshore direction, as well as the usual gravity-wave transients. Our concern is to find radiation boundary conditions which allow these waves to pass through the boundary with the minimum of distortion and reflection. To focus on the performance of the radiation boundary conditions we generate the waves by localized forcing mechanisms in the interior of the computational domain. The major difficulties present in our configuration are that, first, two or more wave modes may approach the boundary simultaneously and, second, the waves generally have the form of dispersing wave packets. Both these factors imply that the phase speed of the waves is not necessarily known in advance, and hence the radiation boundary conditions we consider are of the type introduced by Orlanski [3] (see the discussion below following (1.3)).

There have been several studies of radiation boundary conditions of the Orlanski type. That which is closest to ours is due to Chapman [1], who, for a computational domain similar to ours, studied the merits of several open boundary conditions including those of the Orlanski type. He considered three basic experiments, using the linearized shallow water equations on an f-plane. In the first, a localized sea surface elevation is imposed initially and then relaxes by wave propagation. In the other two experiments a uniform wind stress is imposed, either in the longshore direction or in the cross-shelf direction. He found that the Orlanski radiation boundary condition was generally superior to the alternatives considered. Prior to this, Miller and Thorpe [4] modified the original Orlanski radiation boundary condition, which was proposed for a leapfrog time-stepping scheme, by implementing it instead in the context of upstream differencing. Their procedure is similar to that which we shall adopt in our discussion. They tested their implementation against other variants for an evolving density current and found their method gave some improvement. Camerlengo and O'Brien [5] proposed a simplification of the Orlanski radiation boundary condition appropriate for limited-region oceanic and atmospheric models. They found their version satisfactory for Kelvin waves, but it did not perform so well for Rossby waves. These and other studies have been reviewed by Röed and Cooper [2]. They conclude that ''the response [in the computational domain] is highly sensitive to the implemented open boundary conditions,'' and emphasize the necessity to construct the radiation boundary condition to fit the problem being considered. They also discuss radiation boundary conditions for forced waves (see also Röed and Smedstad [6]) and oblique waves, aspects which we shall not pursue here.

0021-9991/96 $12.00

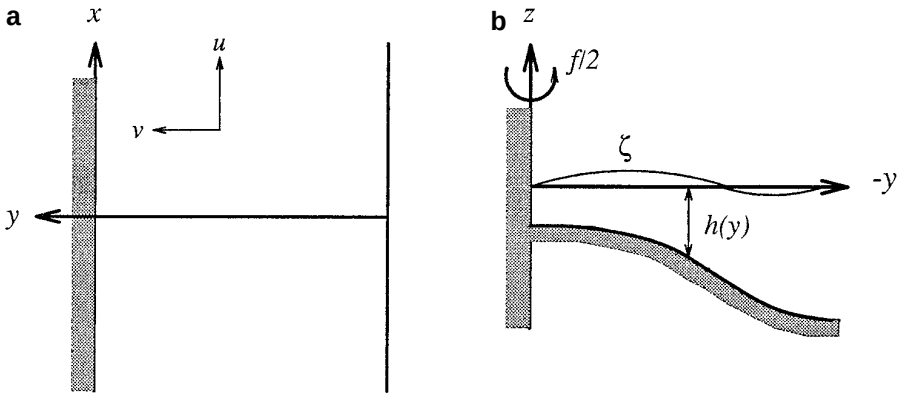

FIG. 1. (a) Computational domain in x, y coordinates. (b) Depth profile.

Next, we introduce the shallow water equations, which are, in standard notation,

$$u_t + uu_x + vu_y - fv + g\zeta_x = \frac{\tau_W^{(x)}}{H}, \tag{1.1a}$$

$$v_t + uv_x + vv_y + fu + g\zeta_y = \frac{\tau_W^{(y)}}{H}, \tag{1.1b}$$

$$\zeta_t + (Hu)_x + (Hv)_y = 0. \tag{1.1c}$$

Here $H = h + \zeta$, (u, v) are the mean velocity components in the along-shelf (x) and cross-shelf (y) directions, f is the Coriolis parameter, g is the gravitational acceleration, $\tau_W^{(x,y)}$ are the wind stress components, $h(y)$ is the undisturbed water depths, and ζ is the free surface elevation. The equations are solved numerically in a rectangular domain (see Figs. 1a, b). One boundary $(y = 0)$ is the coastline, and the contours for the bottom topography are parallel to this boundary, with the depth increasing offshore. For simplicity, we also place a rigid boundary offshore at $y = -W$. In general, this should be an open boundary, but since most of the wave energy is in coastally trapped waves which propagate in the alongshore direction, this simplification is justified here. The boundary conditions at these rigid boundaries are then

$$hv = 0 \quad \text{at } y = 0, -W. \tag{1.2}$$

In the longshore direction, $\zeta, u, v \to 0$ as $|x| \to \infty$ at any finite time. But, in the computational domain, $|x| \le L$ we shall need artificial boundary conditions at $|x| = \pm L$. These will be introduced below. The problem specification is completed by the formulation of initial conditions, and by the specification of the wind stress. This we shall do in Section 3.

On the open boundaries $x = L$ and $x = -L$, we use the conventional radiation boundary condition,

$$\zeta_t + c\zeta_x = 0 \quad \text{at } x = L, -L. \tag{1.3}$$

Here c is the phase speed of a wave approaching the boundary. The crucial question here is the choice of the speed c. In early numerical models c was chosen according to the known wave dynamics of the problem being considered. In the context of the shallow water equations the traditional choice is $c = \sqrt{gh}$, where h is the local water depth (e.g., Wurtele *et al.* [7], Davies and Furnes [8], or Fandry [9]), which corresponds to the assumption that the waves approaching the boundary are surface gravity waves. However, in problems such as the present, where h is a function of y with the consequence that, as well as surface gravity waves, there is a full spectrum of coastally trapped waves, this choice is not appropriate. Instead we follow Orlanski [3] and compute c from values of ζ near the boundary. We consider three implementations of the Orlanski radiation boundary conditions similar to those introduced by Miller and Thorpe [4]. In addition we introduce three new modifications of the Orlanski method.

Before proceeding to describe the numerical implementation of (1.3), we should comment that (1.3) is itself an ad hoc approximation, whose justification is based mainly on the expectation that waves approaching the boundary will be approximately linear, nondispersive and propagating normal to the boundary. Attempts to construct exact radiation boundary conditions, or rational approximations to an exact condition, have been discussed by Engquist and Magda [10] and Keller and Givoli [11] for the two-dimensional wave equation, Hagstrom and Hariharan [12] for the spherically symmetric gas dynamic equations and Higdon [13] for elastic wave propagation. However, even the shallow-water equations (1.3) seem too complex for this approach to be pursued here, and hence our strategy is to regard (1.3) as the given radiation boundary condition and then to examine its numerical implementation. But in doing so we hasten to point out that our method of numerical implementation reveals that (1.3) can be regarded as an interpolation formula (see Röed and Cooper [2]).

In the interior of the computational domain we use a numerical method developed by Tang *et al.* [14] (see also Tang

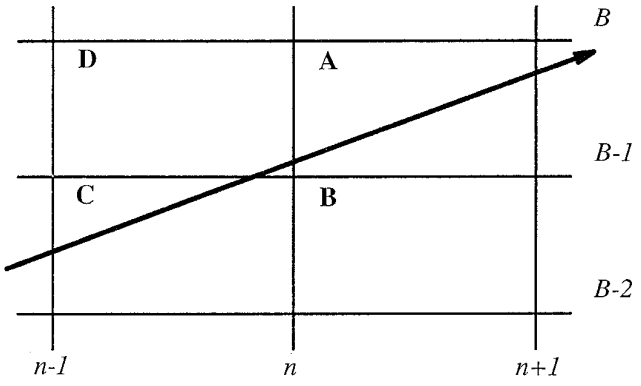

FIG. 2. Grid structure near the boundary.

[15]), which is based on an Arakawa B-grid. It is not our purpose here to discuss the merits or otherwise of this particular numerical scheme, since our focus is on the radiation boundary condition. However, for comparison, some calculations with a numerical scheme similar to that used by Fandry [9], which is based on an Arakawa C-grid, were also carried out with general results similar to those reported here.

In Section 2 we describe the Orlanski radiation boundary conditions and our new modifications. Then in Section 3 we present our numerical tests of these conditions. In Section 4 we summarize our results.

2. RADIATION BOUNDARY CONDITIONS

In this section, various numerical implementations of the radiation boundary condition (1.3) are described. It is sufficient to discuss just $x = L$. Let ζ_i^n denote the value of ζ at $x = x_i$, $y = y_j$, $t = t_n$, where x_i, y_j, t_n are the discretized values of x, y, t, respectively. Then the aim of a discretized version of the radiation boundary condition is to obtain ζ_B^{n+1} from the values of ζ at times t_n, t_{n-1}, ... and the nearby boundary points x_B, x_{B-1}, ... Here x_B denotes the boundary $x = L$, x_{B-1} is the grid point just inside the boundary, and so on (see Fig. 2). Note that in implementing the radiation boundary condition (1.3) we temporarily suppress the dependence on y_j, since (1.3) is effectively a condition in x, t only.

First we describe the Orlanski method. Rather than discretize (1.3) directly, instead, (1.3) is interpreted as a statement that ζ_B^{n+1} is determined by a wave which propagates with a positive speed c in the x-direction. This speed c is not necessarily known *a priori*, but should satisfy the Courant–Friedrich–Lewy stability condition

$$0 < r = \frac{c\,\Delta t}{\Delta x} < 1, \tag{2.1}$$

where $\Delta t = t_{n+1} - t_n$ and $\Delta x = x_i - x_{i-1}$, here assumed to be independent of n and i, respectively. Hence, to first order ζ_B^{n+1} is expected to be linearly dependent on ζ_{B-1}^n and ζ_B^n (i.e., all points in box A), so that

$$\zeta_{B-1}^{n+1} = r\zeta_{B-1}^n + (1 - r)\zeta_B^n. \tag{2.2}$$

Note that the coefficients of ζ_{B-1}^n and ζ_B^n on the right-hand side of (2.2) are chosen to ensure that $\zeta = \text{const}$ satisfies (2.2) and that (2.2) is consistent with (1.3) to first order in Δt and Δx. The Orlanski method now estimates r by utilising (2.2) at points near the boundary. There are three possibilities; either r is estimated from (2.2) by stepping back in both time and space (i.e., $n + 1$, $B \to n$, $B - 1$), which is using box C, or by stepping back only in space (i.e., $n + 1$, $B \to n + 1$, $B - 1$), which is using box B, or by stepping back only in time (i.e., $n + 1$, $B \to n$, B), which is using box D. This approach to the Orlanski method is similar to that used by Miller and Thorpe [4]. Following the notation of Chapman [1], these can be denoted as either ORE, ORE′ (explicit Orlanski condition) or ORI (implicit Orlanski condition). Thus we get

$$r = \begin{cases} \hat{r} & \text{if } 0 < \hat{r} < 1, \\ 0, & \text{if } \hat{r} \le 0, \\ 1, & \text{if } \hat{r} \ge 1, \end{cases} \tag{2.3}$$

where the intermediate value $\hat{r}$ is given by either

$$\text{ORE: } \hat{r} = \frac{\zeta_{B-1}^n - \zeta_{B-1}^{n-1}}{\zeta_{B-2}^{n-1} - \zeta_{B-1}^{n-1}} \tag{2.4a}$$

$$\text{ORI: } \hat{r} = \frac{\zeta_{B-1}^{n+1} - \zeta_{B-1}^n}{\zeta_{B-2}^n - \zeta_{B-1}^n} \tag{2.4b}$$

$$\text{ORE}'\text{: } \hat{r} = \frac{\zeta_B^n - \zeta_B^{n-1}}{\zeta_{B-1}^{n-1} - \zeta_B^{n-1}} \tag{2.4c}$$

Note that since there is no *a priori* guarantee that $\hat{r}$ as determined by (2.4a), (2.4b), or (2.4c) will satisfy the stability condition (2.1), it is necessary to include the limiting condition 0, 1 for r in (2.3) (see Orlanski [3]).

Next an improved modification of the Orlanski boundary condition is one in which ζ_B^{n+1} is linearly dependent on ζ_B^n, ζ_{B-1}^n, and ζ_{B-1}^{n+1} (i.e., all points in box A). With three interpolation points for ζ_B^{n+1} it is now possible to improve the accuracy of the interpolation with respect to Δt, Δx, as well as consistency with (1.3). This aspect is explored later in this section. The simplest method of deriving the required relation is to note that (1.3) implies that near the boundary ζ depends only on $(x - ct)$ and then to require that the linear relation between ζ_B^{n+1} and the interpolating points should be satisfied by an arbitrary quadratic function of $(x - ct)$. The result is

$$\zeta_B^{n+1} = \zeta_{B-1}^n + s(\zeta_B^n - \zeta_{B-1}^{n+1}), \tag{2.5a}$$

where

$$s = \frac{1-r}{1+r}. \tag{2.5b}$$

Note that r is not needed directly here and that it is sufficient to work with s. The intermediate value $\hat{s}$ of s is now estimated directly from (2.5a) and corresponds respectively to either an explicit or an implicit radiation boundary condition, using either the points in box C or box B. The result is denoted by either SRE or SRI,

$$\text{SRE: } \hat{s} = \frac{\zeta_{B-1}^{n} - \zeta_{B-2}^{n-1}}{\zeta_{B-1}^{n-1} - \zeta_{B-2}^{n}} \tag{2.6a}$$

$$\text{SRI: } \hat{s} = \frac{\zeta_{B-1}^{n+1} - \zeta_{B-2}^{n}}{\zeta_{B-1}^{n} - \zeta_{B-2}^{n+1}}. \tag{2.6b}$$

Then the value of s in (2.5a) is given by

$$s = \begin{cases} \hat{s}, & \text{if } 0 < \hat{s} < 1, \\ 1, & \text{if } |\hat{s}| \geq 1, \\ 0, & \text{if } -1 < \hat{s} \leq 0. \end{cases} \tag{2.7}$$

Here the limiting conditions 1, 0 for s correspond to the limiting conditions 0, 1 for r in (2.3).

An alternative modification allows ζ_B^{n+1} to be linearly dependent on ζ_B^n, ζ_{B-1}^n, and ζ_{B-1}^{n-1} (i.e., all points in box D). Proceeding as above, we get a modified Orlanski boundary condition consistent with (1.3), provided that

$$\zeta_B^{n+1} = \zeta_{B-1}^{n-1} + s'(\zeta_{B-1}^{n} - \zeta_B^{n}), \tag{2.8a}$$

where

$$s' = 2r - 1. \tag{2.8b}$$

Here, to estimate s' an implicit scheme is given by

$$\hat{s}' = \frac{\zeta_{B-1}^{n+1} - \zeta_{B-2}^{n-1}}{\zeta_{B-2}^{n} - \zeta_{B-1}^{n}}, \tag{2.9}$$

where now the points are in both boxes B and C. Then the value of s' in (2.8a) is given by

$$s' = \begin{cases} \hat{s}', & \text{if } |\hat{s}'| < 1, \\ 1, & \text{if } \hat{s}' \leq -1, \\ -1, & \text{if } \hat{s} \geq 1. \end{cases} \tag{2.10}$$

Again the limiting conditions -1, 1 for $\hat{s}'$ correspond to the limiting condition 0, 1 for r in (2.3).

Next we estimate the respective errors in these various implementations of the Orlanski radiation boundary condition. Using a Taylor series expansion for ζ_{B-1}^n and ζ_B^n about the point ζ_B^{n+1} we obtain

$$\zeta_{B-1}^{n} = \zeta_B^{n+1} - \Delta t\, \zeta_t - \Delta x\, \zeta_x + \tfrac{1}{2}(\Delta t)^2 \zeta_{tt} + \Delta x\, \Delta t\, \zeta_{xt} + \tfrac{1}{2}(\Delta x)^2 \zeta_{xx} + \cdots, \tag{2.11}$$

$$\zeta_B^{n} = \zeta_B^{n+1} - \Delta t\, \zeta_t + \tfrac{1}{2}(\Delta t)^2 \zeta_{tt} + \cdots. \tag{2.12}$$

From the above formulas, we get

$$\zeta_B^{n+1} = r\zeta_{B-1}^{n} + (1-r)\zeta_B^{n} + \varepsilon \tag{2.13}$$

where

$$\varepsilon = \Delta t\, \zeta_t + r\, \Delta x\, \zeta_x - \tfrac{1}{2}(\Delta t)^2 \zeta_{tt} - r\, \Delta x\, \Delta t\, \zeta_{xt} - \tfrac{1}{2} r (\Delta x)^2 \zeta_{xx} + \cdots.$$

Here ε is the error in the Orlanski interpolation (2.2), and at this stage we have not explicitly used the radiation boundary condition (1.3). But if we now assume that $\zeta_t + c\zeta_x = 0$ (and then also $\zeta_{tt} + c\zeta_{xt} = 0$) is satisfied on the boundary $x = B$, then the above expression for ε becomes

$$\varepsilon = \tfrac{1}{2}(\Delta t)^2 \zeta_{tt} - \tfrac{1}{2} r (\Delta x)^2 \zeta_{xx} + \cdots. \tag{2.14}$$

This shows that Orlanski radiation boundary condition (2.2) has first-order accuracy when r is assumed known and equal to $c\Delta t/\Delta x$ and the open boundary condition $\zeta_t + c\,\zeta_x = 0$ is satisfied. That is, the error ε is second-order in Δx, Δt.

Similarly, for our modifications of the Orlanski boundary condition (2.5) we have

$$\zeta_B^{n+1} = \zeta_{B-1}^{n} + s(\zeta_B^{n} + \zeta_{B-1}^{n+1}) + \varepsilon, \tag{2.15}$$

where

$$\varepsilon = \tfrac{1}{2}(1+s)(\Delta t)^2 \zeta_{tt} + \tfrac{1}{2}(1-s)(\Delta x)^2 \zeta_{xx} + \Delta x\, \Delta t \zeta_{xt} + \cdots \tag{2.16}$$

or

$$\varepsilon = -\frac{1}{2}\frac{(1+s)^2}{(1-s)}(\Delta t)^2 \zeta_{tt} + \frac{1}{2}(1-s)(\Delta x)^2 \zeta_{xx} + \cdots$$

and

$$s = \frac{1-r}{1+r}.$$

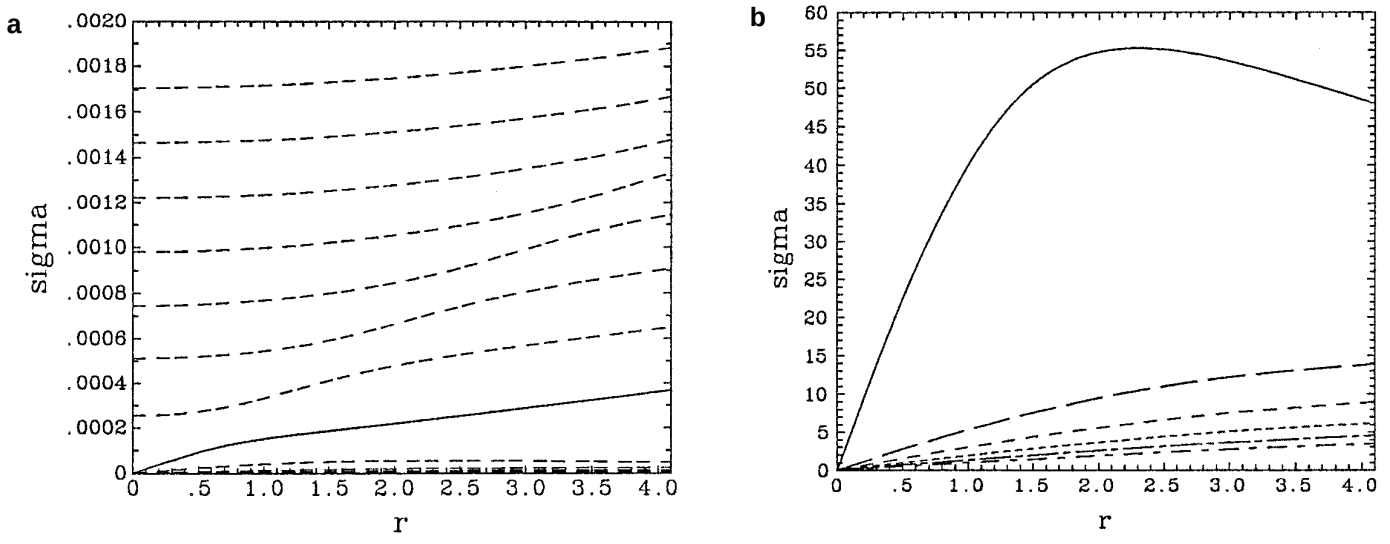

FIG. 3. (a) Dispersion relation for the tanh profile (3.6a) with $\sigma > 0$, where $r = kL/\pi$. The solid line is the Kelvin wave, above it are the edge waves and below are the shelf waves. Note that r is the ''number'' of waves in a domain of length $2L$. (b) As above but only for shelf waves. The solid line is the first mode shelf wave, and below are the second mode etc. Here σ is measured in units of 10^{-6} s^{-1}.

Further, for the modification (2.8) we obtain

$$\zeta_B^{n+1} = \zeta_{B-1}^{n-1} + s'(\zeta_{B-1}^n - \zeta_B^n) + \varepsilon, \tag{2.17}$$

where

$$\varepsilon = -2(\Delta t)^2\zeta_{tt} - \tfrac{1}{2}(1 + s')(\Delta x)^2\zeta_{xx} - (2 + s')\,\Delta x\,\Delta t\zeta_{xt} + \cdots.$$

or

$$\varepsilon = \frac{2}{1 + s'}(\Delta t)^2\zeta_{tt} - \frac{1}{2}(1 + s')(\Delta x)^2\zeta_{xx} + \cdots$$

and

$$s' = 2r - 1.$$

Note that in all cases the error ε is second-order in Δx, Δt, independent of how r or s or s' are determined. But, if we also assume that near the open boundary $\zeta \approx \zeta(x - ct)$ (i.e., $\zeta_t + c\zeta_x = 0$ not only holds on $x = B$ but also in the vicinity of $x = B$), then the Orlanski boundary conditions remain only first-order accurate, but the modified boundary conditions (2.5) and (2.8) become second-order accurate (i.e., ε is third-order in Δx, Δt). Thus the modified radiation boundary conditions (2.5) and (2.8) are an improvement on the Orlanski boundary condition (2.2) and have higher order accuracy, but provided $\zeta \approx \zeta(x - ct)$. Although this is generally not the case, since analysis of the linearized version of the shallow water equations would show that the waves approaching the boundary are dispersing wave packets, it can be expected that when long wavelengths dominate, the solution for each wave mode approximates the form $\zeta \approx \zeta(x - ct)$. Further, for the typical waves generated in storm surge simulations we can expect long wavelengths to dominate.

Importantly this error analysis is independent of how r, s, and s' are determined. This is significant since r, s, and s' are given by ratios of small quantities and, hence, can be expected to be rather noisy. Indeed, our numerical evaluation of these quantities show this. Hence the modified boundary conditions (i.e., SRE etc.) should provide better results than the Orlanski boundary conditions (i.e., ORE etc.). This point distinguishes our approach to the error analysis from that of Miller and Thorpe [4]. They did not assume that $\zeta_t + c\zeta_x = 0$ was satisfied on $x = B$, but instead they inserted the approximate formulas (2.4) for $\hat{r}$ (or (2.6) for $\hat{s}$, or (2.9) for $\hat{s}'$) in ε. Thus, for the Orlanski boundary condition they get

$$\varepsilon = (\Delta t)^2\zeta_{tt} + \Delta x\,\Delta t\,\zeta_{xt} + \hat{r}\,\Delta x\,\Delta t\,\zeta_{xt} + \hat{r}(\Delta x)^2\zeta_{xx}, \tag{2.18}$$

which is second-order. To obtain this result we use a Taylor series expansion for ζ_{B-1}^{n-1} and ζ_{B-2}^{n-1} about the point ζ_B^{n+1} to obtain

$$\begin{aligned}\zeta_{B-1}^{n-1} &= \zeta_B^{n+1} - 2\,\Delta t\,\zeta_t - \Delta x\,\zeta_x + 2(\Delta t)^2\zeta_{tt} \\ &\quad + 2\,\Delta x\,\Delta t\,\zeta_{xt} + \tfrac{1}{2}(\Delta x)^2\zeta_{xx} + \cdots, \\ \zeta_{B-2}^{n-1} &= \zeta_B^{n+1} - 2\,\Delta t\,\zeta_t - 2\,\Delta x\,\zeta_x + 2(\Delta t)^2\zeta_{tt} \\ &\quad + 4\,\Delta x\,\Delta t\,\zeta_{xt} + 2(\Delta x)^2\zeta_{xx} + \cdots.\end{aligned}$$

Then using these and (2.11) for ζ_{B-1}^n in (2.4a) (i.e., ORE) for $\hat{r}$, we obtain

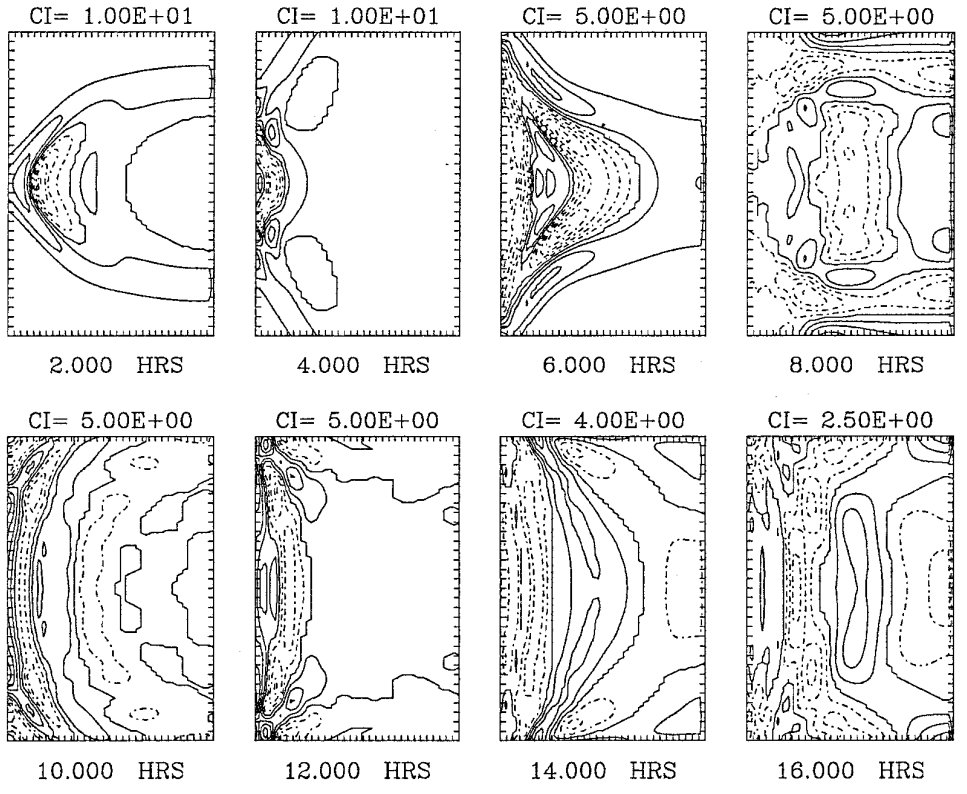

FIG. 4. Contour plots of ζ for the pressure initial condition (3.2) with depth profile (3.6a) and parameters $f = 0$, $R_0 = 75$ km, for the radiation boundary condition SRE.

$$\hat{r} = -\frac{\Delta t\, \zeta_t}{\Delta x\, \zeta_x} + \cdots,$$

or

$$-\hat{r}\,\Delta x\,\zeta_x = \Delta t\,\zeta_t - \tfrac{3}{2}(\Delta t)^2\zeta_{tt} - \Delta x\,\Delta t\,\zeta_{xt} - 2\hat{r}\,\Delta x\,\Delta t\,\zeta_{xt} - \tfrac{3}{2}\hat{r}(\Delta x)^2\zeta_{xx}.$$

Substituting this expression into (2.14) then gets the error ε expressed as (2.18) above. If we now assume also that $\zeta \approx \zeta(x - ct)$ then the error ε in (2.14) or (2.18) becomes third order. A similar analysis can be carried out for ORI, ORE′, SRE, SRI, and SRI′, and in each case ε is second order, but it becomes third order when $\zeta \approx \zeta(x - ct)$ is assumed. Curiously, ε is identically zero at second order for ORE′ as noted by Miller and Thorpe [4]. But we emphasize again that this error analysis uses the interpolation formulas for $\hat{r}$ (2.4a) etc., whereas our error analysis is independent of how r etc. are evaluated. Our numerical results show that the interpolation formula (2.4a) for $\hat{r}$ etc. is very noisy and, hence, we expect our error analysis to be more robust. Further, the implementation of the formula assumes that $\hat{r}$ is given by (2.4a) only when $0 < \hat{r} < 1$ (see (2.7)), whereas the above error analysis assumes (2.4a) holds for all $\hat{r}$.

3. NUMERICAL TESTS

Since the aim here is to test the validity of radiation boundary conditions designed to allow waves to cross the open boundary without reflection or distortion, we generate waves either through an initial-value problem with a localized initial condition given by

$$\zeta = \zeta_0(x, y), \quad u = u_0(x, y), \quad v = v_0(x, y) \quad \text{at } t = 0, \quad (3.1)$$

where the functions ζ_0, u_0, v_0 are effectively nonzero only in the middle part of the domain, or with localized wind stress forcing $\tau_W^{(x,y)}$ which are likewise effectively nonzero only in the middle of the domain.

For the results shown here, we either used an initial condition

$$\zeta_0 = \zeta_m \exp\left(-\frac{x^2}{R_0^2} - \frac{(y + y^0)^2}{R_0^2}\right), \quad u_0 = v_0 = 0, \quad (3.2)$$

corresponding to an input of potential energy, or

$$\zeta_0 = 0, \quad u_0 = \psi_{0y}/h, \quad v_0 = -\psi_{0x}/h, \quad (3.3)$$

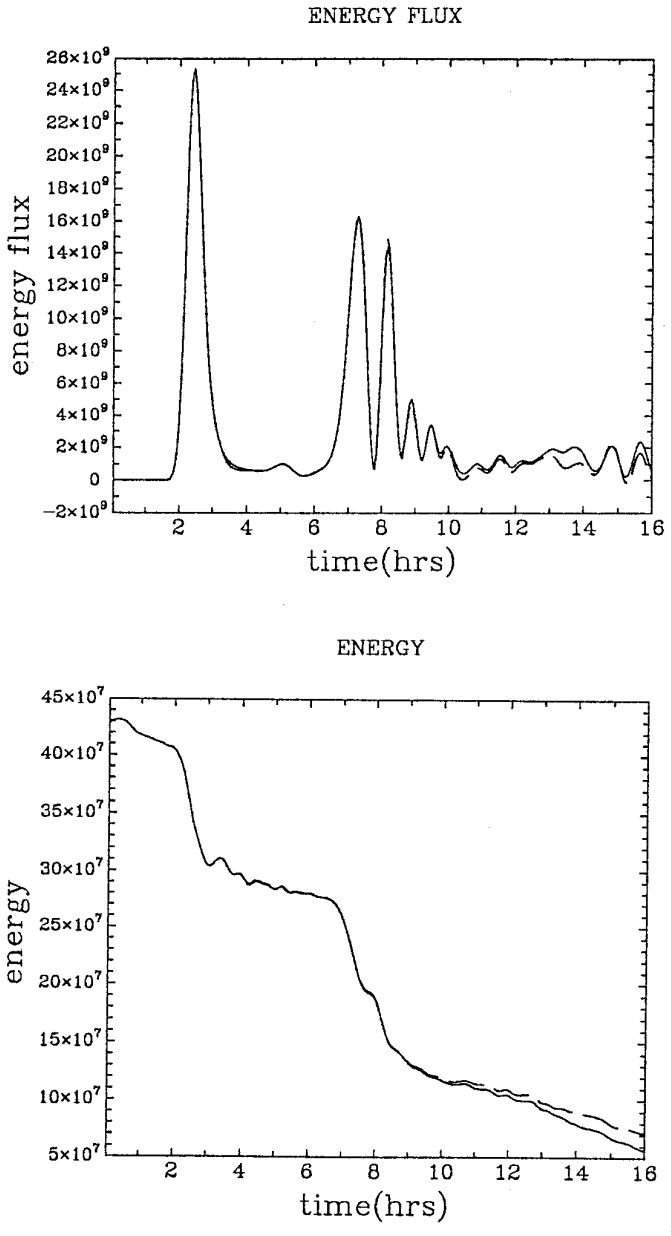

FIG. 5. As for Fig. 4, but the plots of energy flux F for (3.7) and energy E for (3.8), the solid line is the result from the doubling the domain, while the dashed line is the result from the original domain.

where

$$\psi_0 = \psi_m \exp\left(-\frac{x^2}{R_0^2} - \frac{(y+y_0)^2}{R_0^2}\right),$$

corresponding to an input of kinetic energy. In both these cases $\tau_W^{(x,y)}$ are set to zero. The initial condition (3.2) corresponds to a localized pressure disturbance of elevation ζ_m, effective radius R_0, and centred at $x = 0$, $y = -y_0$, while (3.3) corresponds to a localized eddy with maximum radial velocity $V_m = 0.86\psi_m/h_0R_0$, effective radius R_0, and centred at $x = 0$, $y = -y_0$, where $h_0 = h(-y_0)$. Also, the waves generated by an atmospheric wind stress are considered, where we either use a travelling longshore wind stress,

$$\tau_W^{(x)} = \tau_m \exp\left(-\frac{(x-x_1-Vt)^2}{R_0^2} - \frac{(y+y_0)^2}{R_0^2}\right), \qquad \tau_W^{(y)} = 0, \tag{3.4}$$

or a tropical cyclone model (for $f < 0$),

$$\tau_W^{(x)} = \tau_m \exp\left(-\frac{(x-x_1-Vt)^2}{R_0^2} - \frac{(y+y_0)^2}{R_0^2}\right)\frac{(y+y_0)}{R_0}, \tag{3.5a}$$

$$\tau_W^{(y)} = -\tau_m \exp\left(-\frac{(x-x_1-Vt)^2}{R_0^2} - \frac{(y+y_0)^2}{R_0^2}\right)\frac{(x-x_1-Vt)}{R_0}, \tag{3.5b}$$

while ζ_0, u_0, v_0 are set to zero. These both represent a localized wind stress of maximum strength τ_m for (3.4), and $\tau_m(2e)^{-1/2}$ for (3.5), and an effective radius R_0, propagating in the alongshore direction with a speed V from the location $x = -x_1$, $y = -y_0$ to $x = x_0$, $y = -y_0$, in a time $T = (x_0 - x_1)/V$, while τ_m is expressed as $\tau_m = \tau_0 f(t)$. Here $f(t)$ is a smooth function, increasing from zero to unity over a time interval t_1, remaining constant at unity for a time $T - (t_1 + t_2)$ and then decreasing to zero in a time interval t_2. The purpose here is to avoid too much oscillatory behaviour if the wind stress is turned on or off too quickly. Note that for the tropical cyclone model (3.5a), (3.5b) the magnitude of the wind stress is zero at the centre, increases to a maximum at a radius of $R_0 2^{-1/2}$, and then falls off to zero.

In all cases, the disturbance generated outside of the forcing region consists of a set of dispersing coastally trapped wave packets propagating parallel to the coast which eventually reach the open boundaries $x = L$ and $-L$ of the computational domain. Of course, in a realistic storm surge simulation, the wave field generated will be more complicated than that due to the idealized generation mechanisms described here, but it is instructive to test the radiation boundary conditions in relatively simple situations.

The depth profile $h(y)$ is given by either

$$h(y) = h_0 - \Delta h \tanh\left[\frac{b}{W}(y+y_0)\right], \tag{3.6a}$$

or

$$h(y) = h_m + (h_M - h_m)|y/W|. \tag{3.6b}$$

Here, in (1.10b) h_M and h_m are the maximum and minimum

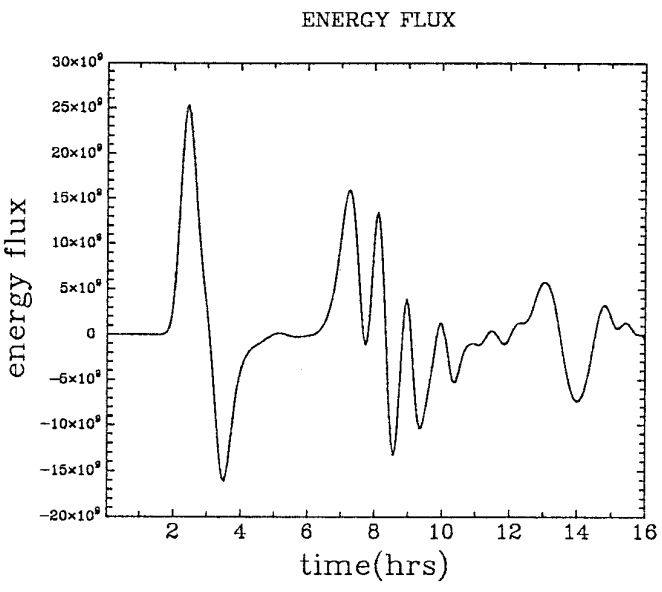

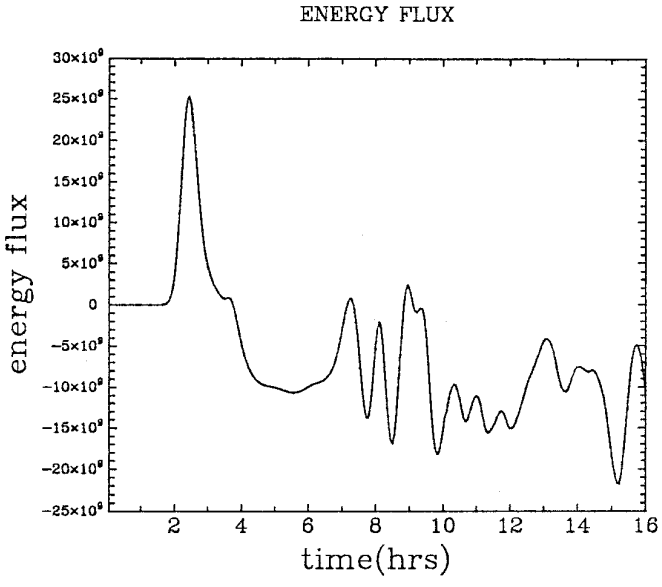

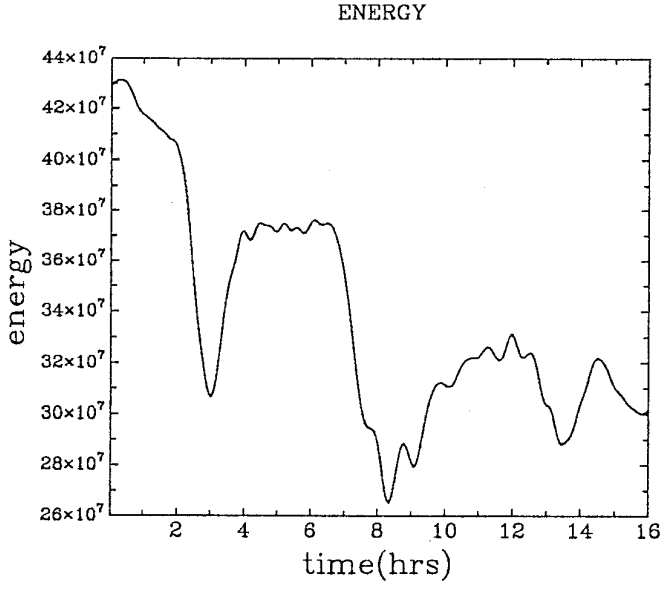

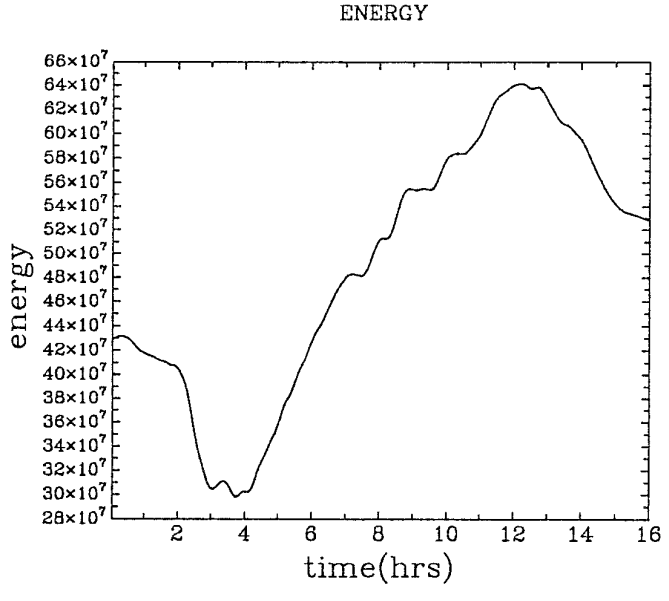

FIG. 6. As for Fig. 5, but the plot of energy flux F and energy E, for the radiation boundary condition ORE′ from the original domain.

FIG. 7. As for Fig. 5, but for the radiation boundary condition (3.12).

depths at $y = -W$ and $y = 0$, respectively. For (3.6a) note that for $y_0 = \frac{1}{2}$ and for $b > 5$ we can effectively put $h_M = h_0 + \Delta h$ and $h_m = h_0 - \Delta h$. In general, the parameter b is a measure of the topographic slope.

Since the parameter space is quite large and limitations allow us to show only some selected representative results, we usually set $L = 600$ km, $W = 400$ km, $y_0 = \frac{1}{2}W$, $h_M = 400$ m, $h_m = 20$ m, and the slope parameter $b = 5.5$ in (3.6a). For the initial conditions (3.2) and (3.3) we typically set $R_0 = 50$ or 75 km, $\zeta_m = 100$ cm, and $V_m = 25$ cm/s, while in (3.4) and (3.5) we set $\tau_m = 100$ or 300 cm^2/s^2, $V = 20$ km/hr, $T = 18$ h, $t_1 = 3$ hr, $t_2 = 3$ h and set $x_1 = -180$ km, $x_0 = 180$ km with $R_0 = 75$ or 100 km.

To test the radiation boundary conditions the energy flux at the open boundary, $x = L$, and the energy in the computational domain are computed. These are defined by

$$F = \int_{-W}^{0} Hu\left(g\zeta + \frac{1}{2}u^2 + \frac{1}{2}v^2\right) dy \quad \text{at } x = L. \tag{3.7}$$

$$E = \int_{-L}^{L}\int_{-W}^{0}\left(\frac{1}{2}H(u^2 + v^2) + \frac{1}{2}g\zeta^2\right) dy\, dx. \tag{3.8}$$

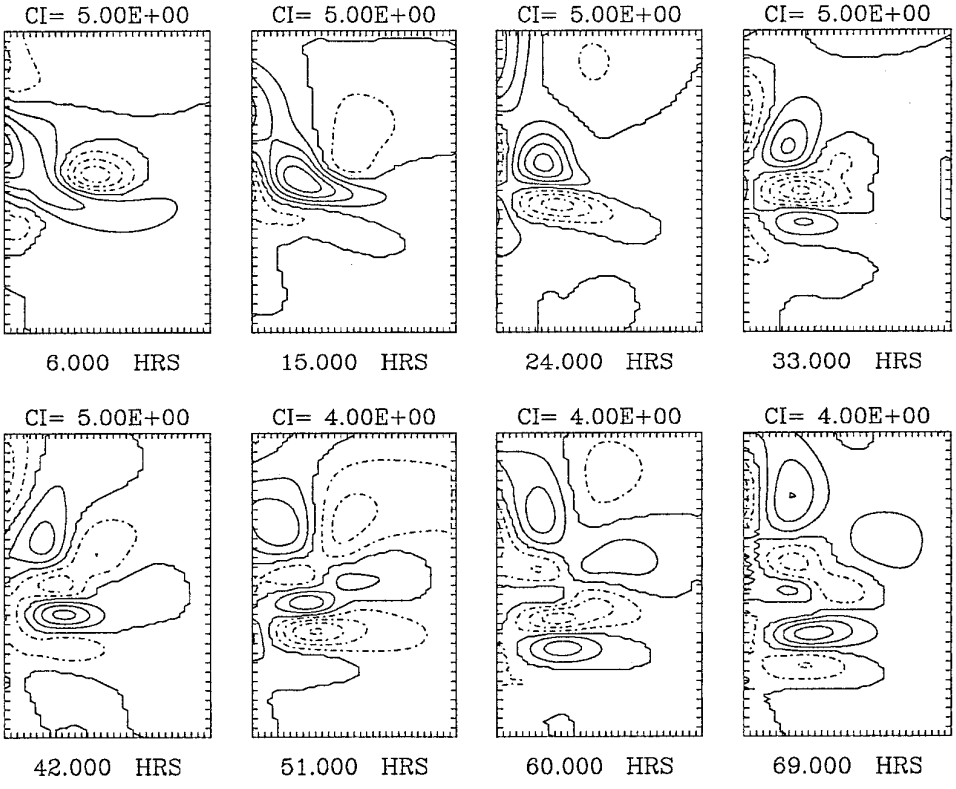

FIG. 8. Contour plots of ζ for the eddy initial condition (3.2) with depth profile (3.6a) and parameters $f = -10^{-4}$, $R_0 = 75$ km, for the radiation boundary condition SRE.

In practice F is computed at a point just inside the boundary $x = L$ to avoid local errors associated with the open boundary condition. In the absence of any wind stress or atmospheric pressure forcing and in the absence of friction, the time rate of change of E should be balanced by F, together with the corresponding energy fluxes at the other open boundaries. Then we double the computational domain in the alongshore direction (i.e., $|x| < 2L$, $0 < y < -W$) and we compare with the corresponding solutions in the same main domain, $|x| < L$, $0 < y < -W$. In particular, we compare F and E.

Based on analysis of the linearized version of the shallow water equations (1.1), we expect the problems defined above to lead to the generation of surface gravity wave transients and coastally trapped waves. These latter take the form of dispersive wave packets propagating in the alongshore direction with a modal structure in the offshore direction. They consist of high-frequency edge waves propagating in both directions and, when the Coriolis parameter $f \neq 0$, lower-frequency Kelvin waves and shelf waves propagating in the positive (negative) x-directions when f is negative (positive). Since the main purpose is to test the effectiveness of the radiation boundary conditions in allowing these coastally trapped waves to propagate out of the domain, we have concentrated here on the boundaries at $x = \pm L$ and note that the boundary at $y = -W$ is a rigid boundary. This has the consequence that Kelvin waves can propagate in both directions, the wave in the positive (negative) x-direction for f negative (positive) being trapped at the coast $y = 0$, with this situation being reversed for the wave trapped at $y = -W$.

First we tested the radiation boundary conditions with exact coastally trapped wave solutions. These satisfy the linearized, unforced version of the shallow water equations (1.1), and are given by

$$(\zeta, u, v) = \mathrm{Re}\{(\phi(y), \bar{u}(y), -i\bar{v}(y)) \exp(-i\sigma t + ikx)\}, \quad (3.9)$$

where k is the alongshore wavenumber (assumed positive) and σ is the wave frequency. Here the modal function $\phi(y)$ satisfies the equation

$$(gh\phi_y)_y + \left(\sigma^2 - f^2 - ghk^2 + \frac{gfk}{\sigma} h_y\right)\phi = 0 \quad \text{in } 0 > y > -W, \quad (3.10a)$$

and

$$\bar{u}(y) = \frac{g}{\sigma^2 - f^2}(\sigma k\phi + f\phi_y), \quad (3.10b)$$

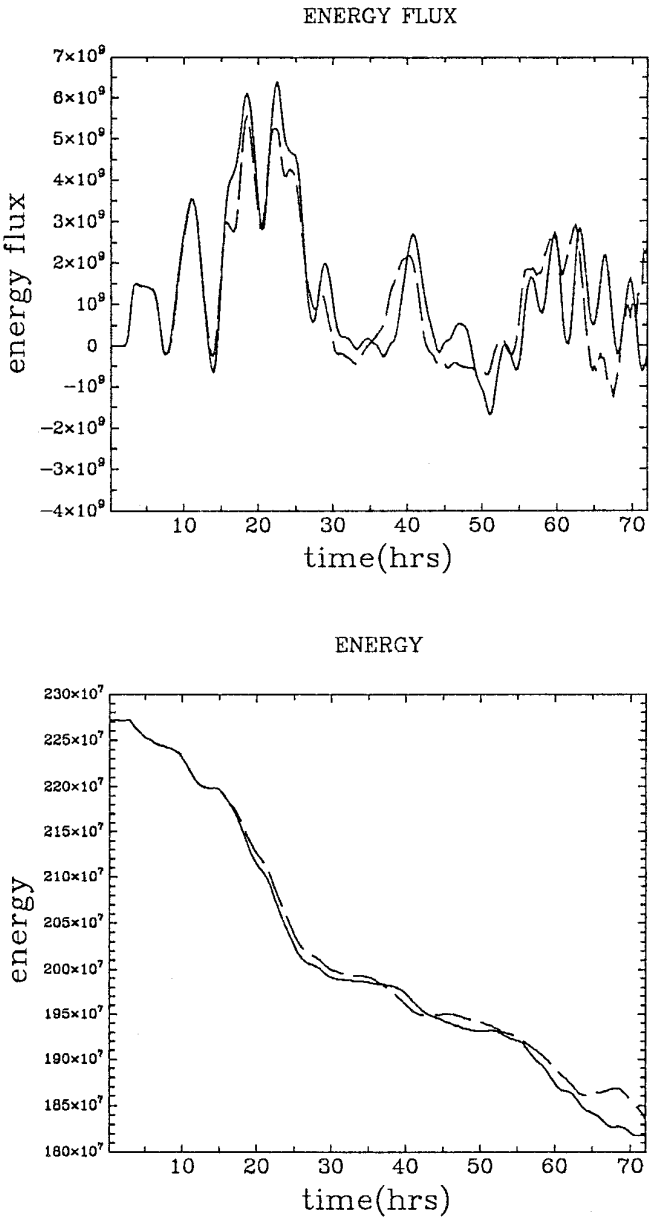

FIG. 9. As for Fig. 8, but the plots of energy flux F for (3.7) and energy E for (3.8). The solid line is the result from doubling the domain, while the dashed line is the result from the original domain.

$$\bar{v}(y) = \frac{g}{\sigma^2 - f^2}(\sigma k \phi_y + f k \phi). \tag{3.10c}$$

The boundary condition (1.2) becomes

$$h\left(\phi_y + \frac{fk}{\sigma}\phi\right) = 0 \quad \text{at } y = 0, -W. \tag{3.11}$$

Equations (3.10a) and (3.11) define an eigenvalue problem for σ, with parameter k and corresponding eigenfunction $\phi(y)$, but we note that σ occurs nonlinearly in (3.9). A typical set of dispersion curves are shown in Fig. 3 for the "tanh" depth profile (3.6a) with $f = -10^{-4}\,\mathrm{s}^{-1}$. Here we show only the waves propagating in the positive x-direction. There is an infinite set of edge waves where $|\sigma| > |f|$, a Kelvin wave, and an infinite set of shelf waves with $|\sigma| < |f|$. In the negative x-direction there is an infinite set of edge waves and a Kelvin wave, both being similar to their counterparts in the positive x-direction. But note that the Kelvin wave propagating in the positive (negative) x-direction is trapped at the boundary $y = 0\,(-W)$, respectively, when $f < 0$, the situation being reversed for $f > 0$. The radiation boundary conditions were then tested using the linearized, unforced version of the shallow water equations (1.1) and using (3.9) with $t = 0$ as an initial condition. To avoid complications from the bottom boundary $x = -L$, we multiplied these analytical solutions by an envelope function $F(x)$, which is a smooth function effectively equal to 1 for $x > 0$ and 0 for $x < -L$. Tests with these one-sided wave packets for a range of wavenumbers k showed that all the radiation boundary conditions allowed the wave to pass through the open boundary with no detectable change in speed or shape, at least until the rear of the wave packet reached $x = L$.

Next we turn to our numerical results using the more general initial conditions (3.2), or (3.3). Figure 4 shows the results with $f = 0$, for the pressure initial condition (3.2) with the "tanh" depth profile (3.6a). The parameter setting is $L = 600$ km, $W = 400$ km, $y_0 = \frac{1}{2}W$, $h_M = 400$ m, $h_m = 20$ m, $b = 5.5$, and $R_0 = 75$ km, $\zeta_m = 100$ cm. Similar results are obtained with $f = -10^{-4}\,\mathrm{s}^{-1}$, but they will not be shown here (see Tang [15]). The figure shows the contour plots of surface elevation ζ, and it clearly shows the development of edge waves propagating in both alongshore directions. The corresponding plots for u and v show a similar situation (see Tang [15]). This result is for the SRE radiation boundary condition. The corresponding energy flux F (3.7) and energy E (3.8) are shown in Fig. 5 (in fact we plot $F/\Delta y$ and $E/\Delta x\ \Delta y$). From the figure for F we identify a burst of surface gravity wave transients reaching $x = L$ at about 2–3 h, followed by edge waves at about 7–8 h. The corresponding decreases in energy E are well correlated with these energetic bursts of wave activity. In this case, there is no evidence of wave reflection from the boundaries $x = \pm L$ for the modified radiation boundary conditions SRE, SRI, SRI′ and the Orlanski boundary conditions ORE, ORI, while the second-order radiation boundary conditions are found to perform a bit better than the first-order boundary conditions, mainly with respect to the passage of the small-amplitude trailing oscillations (see Fig. 5 for times greater than 10 h). Further, the corresponding results from doubling the computational domain are again almost identical (see Fig. 5 for the SRE result). However, when the same problem is considered for ORE′, Fig. 6 shows that this boundary condition cannot cope with any kind of wave propagating to the boundary, since strong reflection happens as soon as waves approach the boundary. The reason

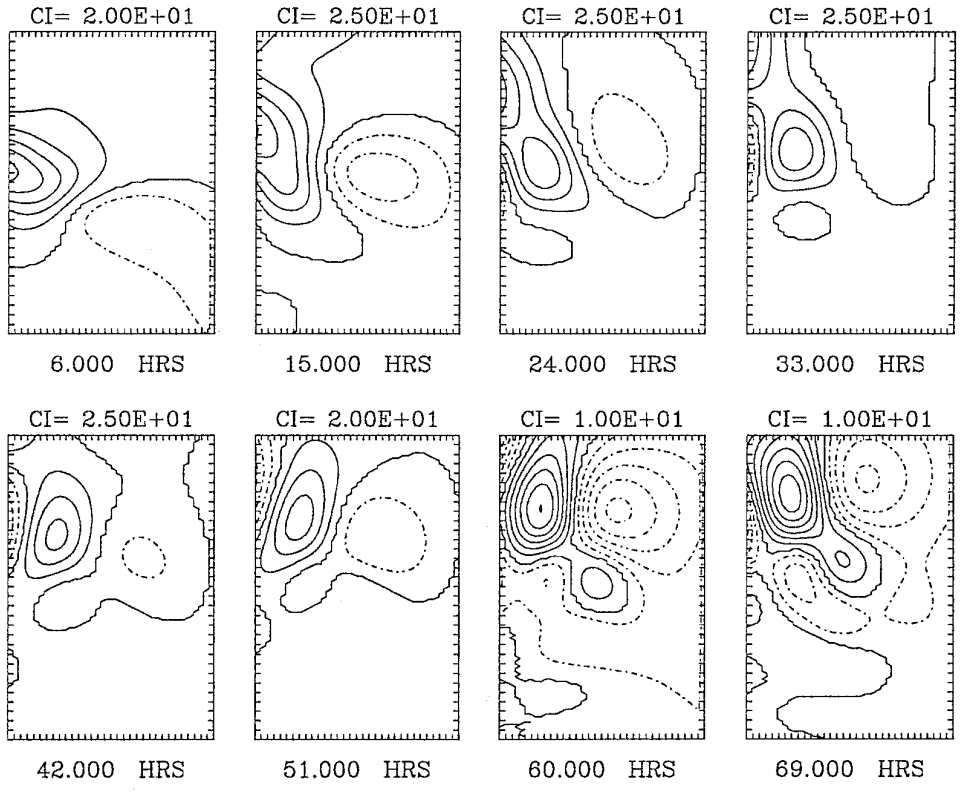

FIG. 10. Contour plots of ζ for the wind stress forcing (3.4) with depth profile (3.6a) and parameters $f = -10^{-4}$, $R_0 = 100$ km, $t_1 = 3$ h, and $t_2 = 6$ h for the radiation boundary condition SRE.

for this is because ORE′ uses box D for the evaluation of $\hat{r}$ (see Fig. 2), which can be regarded as using adjacent boundary values rather than interior values.

Miller and Thorpe [4] pointed out that a linear combination of the three first-order boundary conditions in Section 2,

$$\hat{r} = \hat{r}(\text{ORE}') + \hat{r}(\text{ORI}) - \hat{r}(\text{ORE}), \qquad (3.12)$$

will give a higher order accuracy. This is technically correct, but it does not lead to a better practical result. We tested this radiation boundary condition as well. The results clearly show in Fig. 7 that, after the gravity waves reach the boundary, strong reflection occurs. The reason for this is the inadequacy of ORE′, discussed above.

Next, we show the results for $f = -10^{-4}$ s^{-1} for the eddy initial condition (3.3) and the bottom profile (3.6a). The parameter setting again is $L = 600$ km, $W = 400$ km, $y_0 = \frac{1}{2}W$, $h_M = 400$ m, $h_m = 20$ m, $b = 5.5$, and $R_0 = 75$ km, $\psi_m = 4.5 \times 10^{12}$ cm^3/s. Figure 8 shows contour plots of pressure ζ, and in Fig. 9 we plot the energy flux F and energy E. These results are again for the SRE radiation boundary condition. The surface gravity wave transients are now negligible, while the edge waves are discernible but not quite as significant as the Kelvin wave which reaches $x = L$ at about 4 h, followed by the shelf

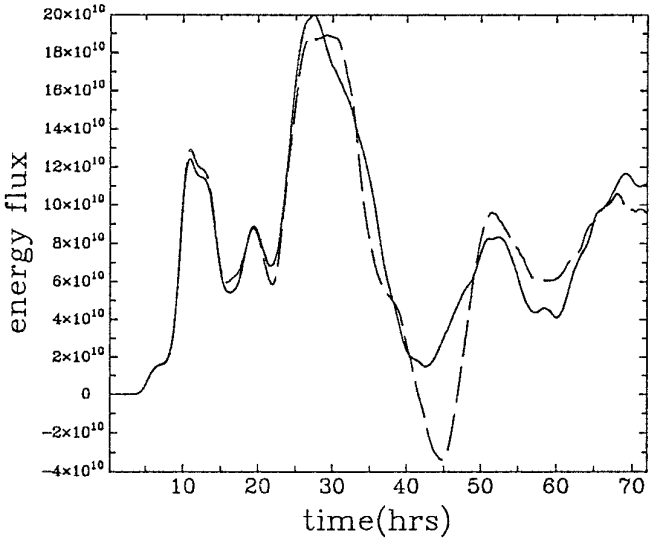

FIG. 11. As for Fig. 10, but the plots of energy flux F. The solid line is the result from the doubling the domain, while the dashed line is the result from the original domain.

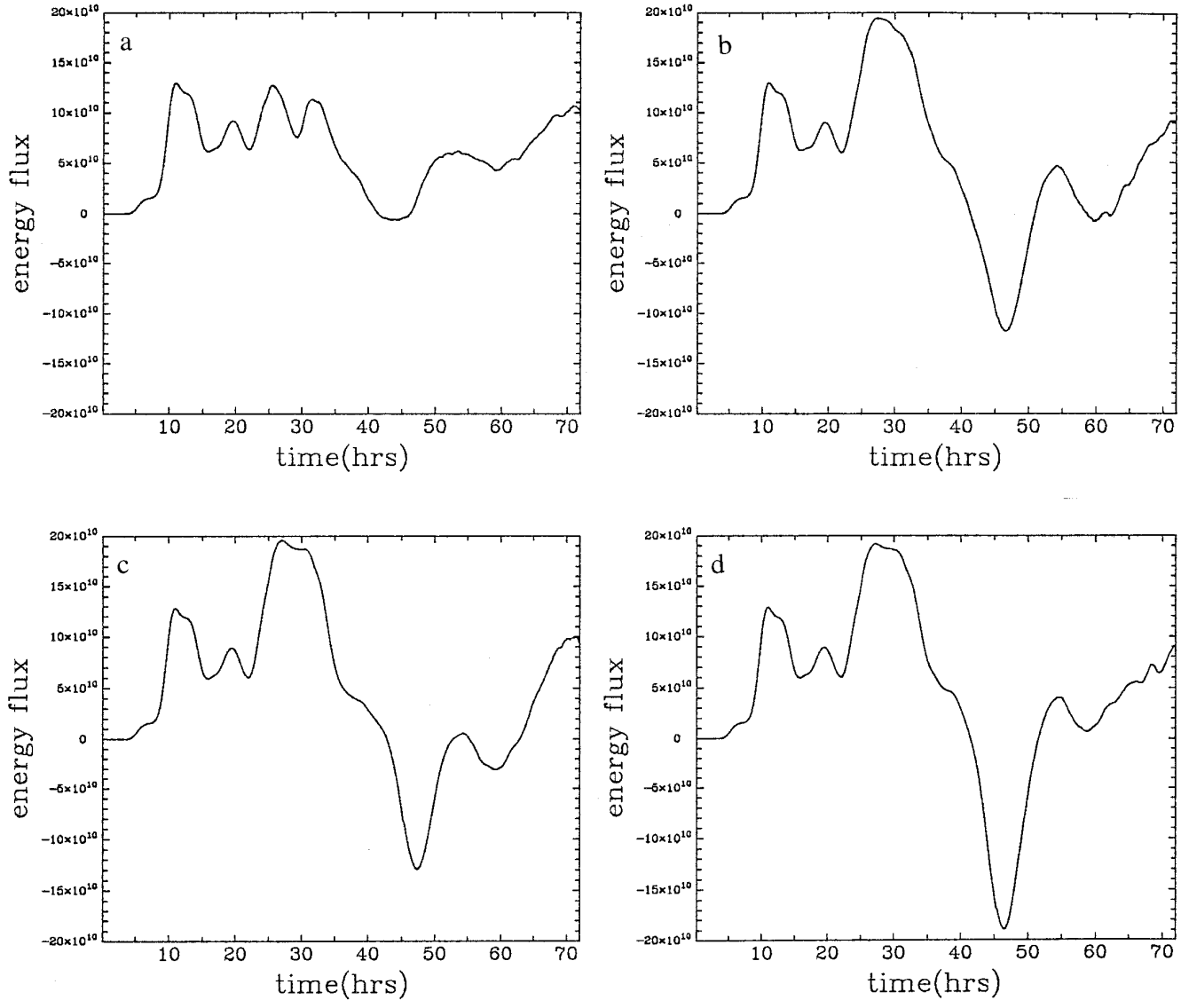

FIG. 12. As for Fig. 11 the plot of energy flux F, but for radiation boundary conditions SRI (a), SRI′ (b), ORE (c), and ORI (d) from the original domain.

waves which now carry most of the energy flux. When we consider the corresponding results obtained from doubling the domain, we find that in this case the radiation boundary conditions SRE, SRI, and SRI′ give comparable and reasonably good results, although again with a marginal bias in favour of SRE. The most serious degradation in performance occurs when a second mode shelf wave arrives at the boundary. The Orlanski boundary conditions ORE and ORI do not perform as well as the modified boundary conditions, particularly for the shelf waves. We also tested the radiation boundary condition ORE′ and Miller and Thorpe's boundary condition (2.31), but again we found that they give very poor results. If we reduce R_0 from 75 km to 50 km, we find basically similar conclusions, although in this case there is a degradation in the performance of all the radiation boundary conditions, and the Orlanski boundary conditions ORE and ORI give even worse results. The reason for this is because the second mode shelf wave now is much stronger than the first mode. Further details can be found in Tang [15].

Now we show the results for wind stress forcing (3.4) for the bottom profile (3.6a). Again we use the same parameters as above but we set $R_0 = 100$ km, $\tau_m = 100$ cm^2/s^2, $V = 20$ km/h, $T = 18$ h, $t_1 = 3$ h, $t_2 = 6$ h, and $x_1 = -180$ km, $x_0 = 180$ km. Figure 10 shows the contour plots of pressure ζ; in Fig. 11 we show the corresponding results for energy flux F for the SRE radiation boundary condition; and Fig. 12 shows the corresponding results for the radiation boundary conditions SRI, SRI′, ORE, and ORI. The energy flux peak at about $t = 12$ h is best interpreted as a mixture of an edge wave and a Kelvin wave, and this is followed by substantial shelf waves. In

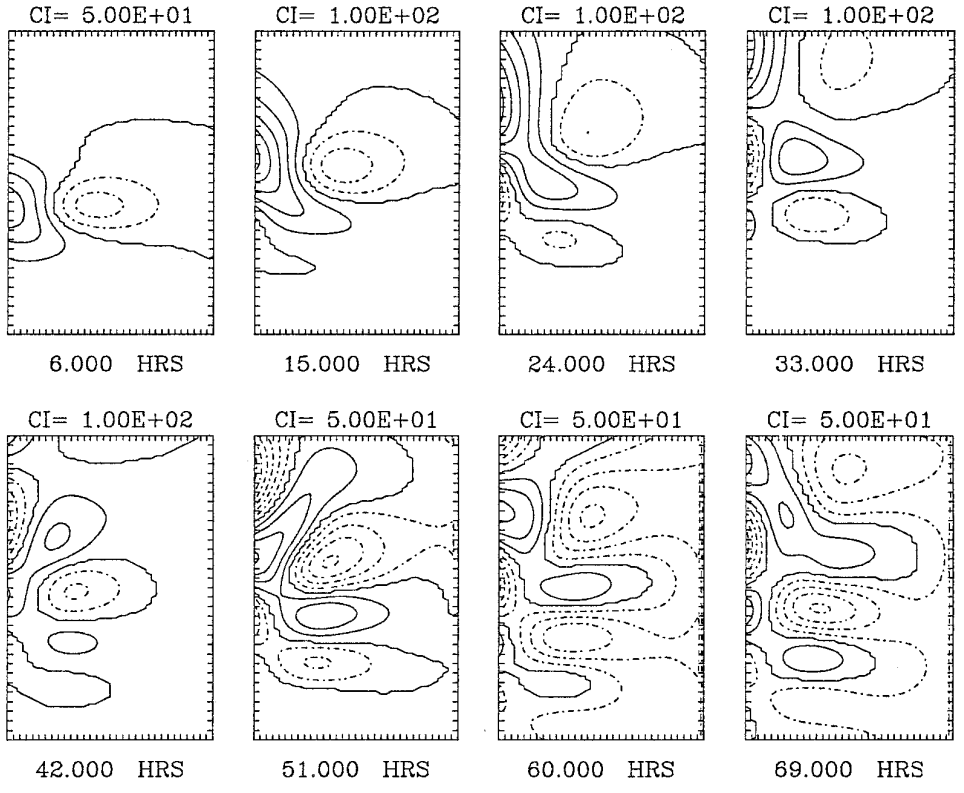

FIG. 13. Contour plots of ζ for the tropical cyclone model (3.5a), (3.5b) with depth profile (3.6a) and parameters $f = -10^{-4}$, $R_0 = 100$ km, $t_1 = 3$ h, and $t_2 = 3$ h for the radiation boundary condition SRE.

this case, all the radiation boundary conditions give comparable results with the doubled domain before the second mode shelf wave arrives at the boundary, except SRI, and none of the radiation boundary conditions deal very satisfactorily with the second mode shelf wave; but again SRE performs the best. When $t_2 = 6$ h, that is, when we turn off the wind stress forcing more smoothly, we get more coherent waves, rather than the more oscillatory waves due to the sudden turning off of the wind stress forcing. Consequently the results for $t_2 = 6$ h agree better with the doubled domain results (see Tang [15]).

Finally we turn to the results for the tropical cyclone model (3.5a), (3.5b), again using the bottom profile (3.6a), with the same domain parameters as before, while the parameters for the wind stress forcing are $R_0 = 100$ km, $\tau_m = 300$ cm^2/s^2, $V =$ 20 km/h, $T = 18$ h, $t_1 = 3$ h, $t_2 = 3$ h, and $x_1 = -180$ km, $x_0 = 180$ km. Figure 13 shows the contour plots of pressure ζ, and in Fig. 14 we show the corresponding results for energy flux F and energy E, again for the SRE radiation boundary condition. This wind stress forcing models a tropical cyclone and we find that it mainly generates shelf waves. Again the radiation boundary conditions SRE performs best, although now SRI is quite similar (see Fig. 14) while the Orlanski radiation boundary conditions ORE, ORI again cannot cope with the second mode shelf wave, giving strong reflection after it reaches the boundary. For more details on this case see Tang [15].

From the above discussion we can draw the simple conclusion that the modified radiation boundary conditions SRE, SRI, and SRI′ perform better than Orlanski radiation boundary conditions ORE, ORI, and we marginally favour SRE. All the radiation boundary conditions have difficulty dealing with the shelf waves, especially the second mode shelf wave, possibly because it tends to be more dispersive.

Further, comparing the radiation boundary condition ORE′ and (3.12) with the other five radiation boundary conditions, we find that ORE′ and (3.12) are not satisfactory and generally give poor results.

In addition, we tested the radiation boundary conditions for the linear bottom profile (1.10b) with the other parameter settings the same as before. Here for this slope we put $h_m = 2$ cm and $h_M = 400$ m. In general we find the same conclusions as above, although the results are different in detail (see Tang [15] for details).

We also tested the radiation boundary conditions with increased amplitudes for the initial conditions and forcing terms in order to test the role of the nonlinear terms. For the pressure initial condition (3.2) with the "tanh" bottom profile (3.6a), if we use the same parameter settings as before, we get almost

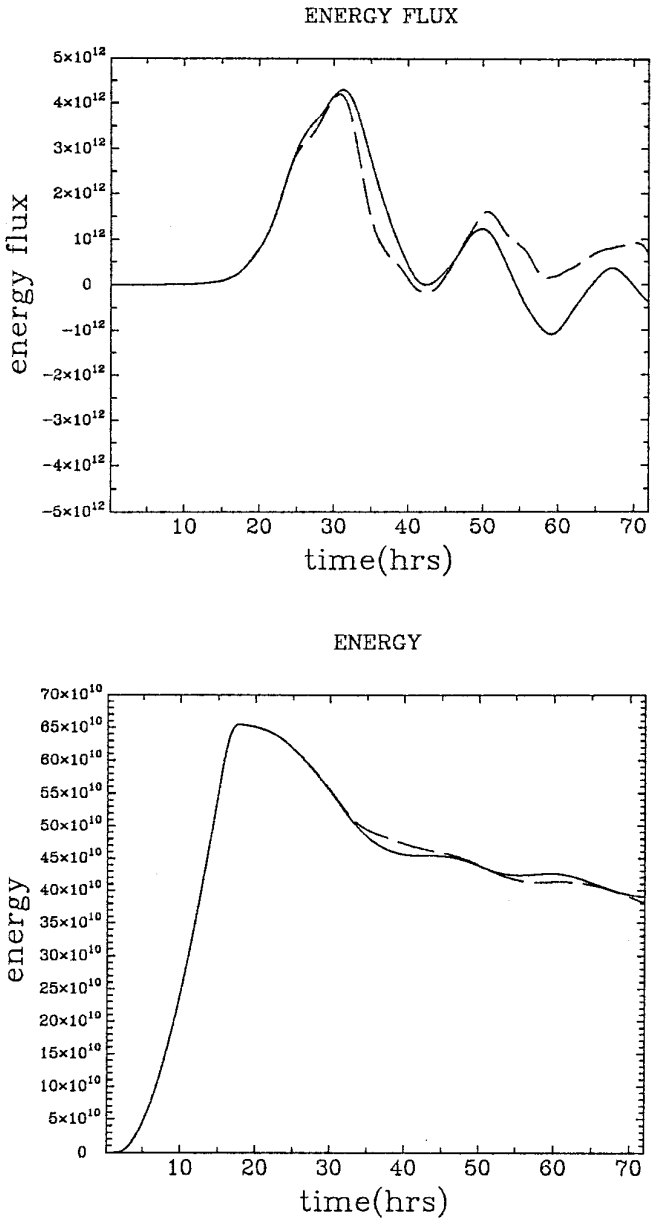

FIG. 14. As for Fig. 13 but the plots of energy flux F for (3.7) and energy E for (3.8). The solid line is the result from the doubling the domain, while the dashed line is the result from the original domain.

identical results to the linear problem (i.e., Eqs. (1.1a)–(1.1c) with the nonlinear terms omitted). We then increased ζ_m to 10 m, which is very large and may be unrealistic, but we still obtained essentially the same results.

For the eddy initial condition (3.3), we find that increasing the initial amplitude of the eddy results in more nonlinear behaviour for the eddy itself, but less wave activity. This aspect we have discussed elsewhere (Grimshaw *et al.* [16, 17]).

We also considered the wind stress forcing (3.4) with τ_m increased to 200 cm^2/s^2, and the other parameter settings the same as before. Compared with the case $\tau_m = 100$ cm^2/s^2 shown in Figs. 10 and 11 we found similar results, but as we increase the forcing, more energy is transferred to the second peak, which corresponds to the shelf wave, and there is less oscillation after this peak. The radiation boundary condition (SRE here) performs just as well when the forcing amplitude is increased. For the tropical cyclone model the results for changing the forcing amplitude are similar and discussed in detail in Tang [15].

4. SUMMARY

In this paper we have examined three versions (2.4a)–(2.4c) of the Orlanski radiation boundary conditions, as well as three new modifications (2.6a), (2.6b), (2.9). These have been tested in the context of the shallow water equations in configurations related to storm surge simulations. Thus we have concentrated on the ability of the radiation boundary conditions to transmit coastally trapped waves. Importantly, we have used either localized initial conditions or forcing mechanisms, which remain localized within the interior of the computational domain, in order to focus on the transmission of freely propagating waves. Thus we do not here consider the issue of the transmission of forced waves. Also, here we do not consider the issue of oblique waves, since the variable bottom topography in the cross-shelf direction has the effect of guiding the waves in the alongshore direction.

Of the six radiation boundary conditions tested, only ORE′ (and (3.12)) was totally unsatisfactory. Of the remaining conditions we find that the modified radiation boundary conditions SRE, SRI, and SRI′ perform better than the Orlanski radiation boundary conditions ORE, ORI. Further, overall, SRE gave marginally the best performance. But all the conditions have difficulties with the shelf waves, particularly for the more dispersive second mode. Indeed, we can infer from our results that the more the waves have the structure of dispersive wave packets, the poorer the performance of all the radiation boundary conditions. But, that having been admitted, our results show that at least for the time span considered here (up to three days) either of the two modified radiation boundary conditions SRE, SRI can be confidently used in storm surge simulations.

The numerical model used here is a two-dimensional, or depth-integrated, storm surge model. But we would not anticipate any major difficulty in incorporating the radiation boundary conditions tested here into three-dimensional models, provided that the fluid is assumed homogeneous and the nomenclature three-dimensional refers to the allowance for vertical shear in the horizontal currents due to parameterised eddy viscosities. However, the development of radiation boundary conditions analogous to those considered here for density-stratified storm surge models remains a topic for future investigation.

ACKNOWLEDGMENTS

This research was supported by ARC Grant A89030441.

REFERENCES

1. D. C. Chapman, *J. Phys. Ocean.* **15,** 1060 (1985).
2. L. P. Roëd and C. K. Cooper, ''Open Boundary Conditions in Numerical Ocean Models,'' in *Advanced Physical Oceanographic Numerical Modelling,* edited by J. J. O'Brien (Reidel, Dordrecht, 1986), p. 411.
3. I. Orlanski, *J. Comput. Phys.* **21,** 251 (1976).
4. M. J. Miller and A. J. Thorpe, *Q. J. R. Meteorol. Soc.* **107,** 615 (1981).
5. A. L. Camerlengo and J. J. O'Brien, *J. Comput. Phys.* **35,** 12 (1980).
6. L. P. Roëd and O. M. Smedstadt, *SIAM J. Sci. Stat. Comput.* **5,** 414 (1984).
7. M. G. Wurtele, J. Paegle, and A. Sielecki, *Mon. Weather Rev*. **99,** 537 (1971).
8. A. M. Davies and G. K. Furnes, *J. Phys. Ocean.* **10,** 237 (1980).
9. C. B. Fandry, *Aust. J. Mar. Freshwater Res.* **32,** 9 (1981).
10. B. Engquist and A. Majda, *Math. Comput.* **31,** 629 (1977).
11. J. B. Keller and D. Givoli, *J. Comput. Phys.* **82,** 172 (1989).
12. T. Hagstrom and S. I. Hariharan, *Math. Comput.* **51,** 581 (1988).
13. R. L. Higdon, *SIAM J. Numer. Anal.* **27,** 831 (1990).
14. Y. Tang, W. Sun, and S. Feng, ''A Method of Separating Current of the Three-Dimensional Shallow Water Hydrodynamical Model,'' in *Storm Surges: Observations and Modelling, Proc. Int. Symp. on Storm Surges, Beijing 1987,* edited by J. Chao, T. S. Murty, C. Bao, M. I. El-Sabh, and F. Liu (1990), p. 49.
15. Y. Tang, Ph.D. thesis, Monash University, 1994 (unpublished).
16. R. Grimshaw, D. Broutman, X. He, and P. Sun, *J. Phys. Ocean.* **24,** 1587 (1994).
17. R. Grimshaw, Y. Tang, and D. Broutman, *Geophys. Astrophys. Fluid Dyn.* **76,** 43 (1994).